Designing thermally stimulated 1.06 mu m Nd3+ emission for the second bio-imaging window demonstrated by energy transfer from Bi3+ in La-, Gd-, Y-, and LuPO4

Lyu, Tianshuai; Dorenbos, Pieter

DOI
10.1016/j.cej.2019.04.125

Publication date
2019

Document Version
Final published version

Published in
Chemical Engineering Journal

Chemical Engineering Journal 372 (2019) 978–991

Contents lists available at ScienceDirect

Chemical Engineering Journal

journal homepage: www.elsevier.com/locate/cej

Designing thermally stimulated 1.06 μm Nd^{3+} emission for the second bio-imaging window demonstrated by energy transfer from Bi^{3+} in La-, Gd-, Y-, and $LuPO_4$

Tianshuai Lyu*, Pieter Dorenbos

Delft University of Technology, Faculty of Applied Sciences, Department of Radiation Science and Technology, Section Luminescence Materials, Mekelweg 15, 2629JB Delft, The Netherlands

HIGHLIGHTS

- A general methodology to rationally design infrared afterglow between ~900–1700 nm.
- New combination of energy transfer of $Bi^{3+} \rightarrow Nd^{3+}$ and adjustable hole trap depth.
- Bi^{3+} as deep electron trap and recombination luminescence centre.
- Our work shows a new general technique to deep understand afterglow mechanisms.
- Explore afterglow phosphor in a design way instead of by trial-and-error approach.

GRAPHICAL ABSTRACT

A general methodology to the rational design of thermally stimulated short-wave infrared (SWIR) luminescence between ~900 and 1700 nm is achieved by a new combination of using efficient energy transfer from Bi^{3+} to Nd^{3+} and an adjustable hole trap depth via valence band engineering.

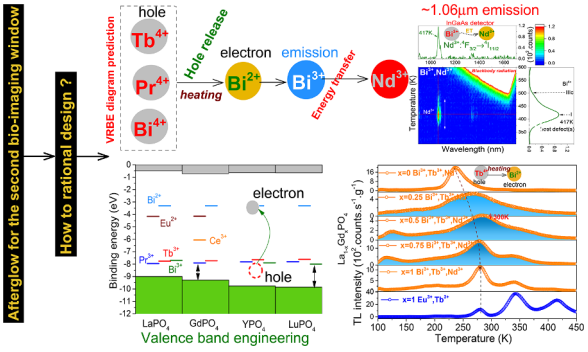

ARTICLE INFO

Keywords:
Bismuth
Valence band engineering
Hole release
Energy transfer
Afterglow

ABSTRACT

We report a general methodology to the rational design of thermally stimulated short-wave infrared (SWIR) luminescence between ~900 and 1700 nm by a new combination of using efficient energy transfer from Bi^{3+} to Nd^{3+} and an adjustable hole trap depth via valence band engineering. Predictions from a vacuum referred binding energy (VRBE) diagram are combined with the data from optical spectroscopy and thermoluminescence to show the design concept by using bismuth and lanthanide doped rare earth *ortho*-phosphates as model examples. Nd^{3+} with its characteristic $^4F_{3/2} \rightarrow {}^4I_j$ (j = 9/2, 11/2, 13/2) emission in the SWIR range is first selected as the emitting centre. The energy transfer (ET) processes from Bi^{3+} or Tb^{3+} recombination centres to Nd^{3+} are then discussed. Photoluminescence results show that the energy transfer efficiency of $Bi^{3+} \rightarrow Nd^{3+}$ appears to be much higher than of $Tb^{3+} \rightarrow Nd^{3+}$. To exploit this ET, thermally stimulated Bi^{3+} A-band emission can then be designed by using Bi^{3+} as a ~2.7 eV deep electron trap in YPO_4. By combining Bi^{3+} with Tb^{3+}, Pr^{3+}, or Bi^{3+} itself, the holes trapped at Tb^{4+}, Pr^{4+}, or Bi^{4+} will release earlier than the electrons captured at Bi^{2+}. On recombination with Bi^{2+}, Bi^{3+} in its excited state is formed generating Bi^{3+} A-band emission. Due to the ET of $Bi^{3+} \rightarrow Nd^{3+}$ 1.06 μm Nd^{3+} emission appears in YPO_4. Herein, the thermally stimulated Nd^{3+} SWIR emission is achieved by hole release rather than the more commonly reported electron release. The temperature when thermally stimulated Nd^{3+} SWIR emission appears can further be engineered by changing the Tb^{3+} or Pr^{3+} hole trap depth in $Y_{1-x}Lu_xPO_4$ by adjusting x. Such valence band engineering approach can also be applied to other

* Corresponding author.
E-mail address: T.lyu-1@tudelft.nl (T. Lyu).

https://doi.org/10.1016/j.cej.2019.04.125
Received 22 February 2019; Received in revised form 2 April 2019; Accepted 19 April 2019
Available online 20 April 2019

compounds like $La_{1-x}Gd_xPO_4$ and $Gd_{1-x}La_xAlO_3$ solid solutions. Our work opens the avenue to motivate scientists to explore novel SWIR afterglow phosphors in a design way instead of by trial and error approach.

1. Introduction

Afterglow is known as a self-sustained luminescence phenomenon [1–3], where a material is capable of first storing excitation energy [4], and then emitting photons for a particular time after removing the excitation source [5,6]. This phenomenon has promising applications in various fields [7], including but not limited to information storage [8], traffic signage [9], and alternating current driven LED (AC-LED) [10]. Particularly, nanoscale infrared afterglow probes, with the advanced application in vivo bio-imaging, have attracted ever-increasing attention [11]. One of the famous examples is the $ZnGa_2O_4:Cr^{3+}$ afterglow nano-probe [12], which shows infrared emission from 650 to 750 nm.

Short-wave infrared (SWIR) light with the emission wavelength between ~900–1700 nm exhibits unique spectral properties such as reduced Rayleigh scattering, which lead to many promising applications like in anti-counterfeiting, military night-vision surveillance, and medical imaging [7,13–16]. For instance, as compared with the near-infrared light with emission wavelength between ~700 and 900 nm, the SWIR light has higher penetration ability in a challenging atmosphere condition like dust, smog, fog, or rain. The SWIR range is in the second bio-imaging window, which shows promising application to arrive at super-sensitive and deep penetration medical bio-imaging. Hong *et al.* [17] reported a type of in vivo fluorescence imaging using Ag_2S quantum dots with adjustable photoluminescence in the ~1100–1400 nm second near-infrared bio-imaging window. With this quantum dots based technique, however, in situ continuous 808 nm laser excitation is required during the optical imaging process, which not only causes tissue auto-fluorescence but also inevitably induces damage to the healthy tissues [18].

Currently, short-wave infrared (SWIR) afterglow luminescence between ~900–1700 nm has attracted research interest. The "self-sustained" SWIR afterglow emission without real-time external excitation not only shows higher penetration in biological tissue compared with the infrared spectral range between ~700–900 nm, but also allows the imaging to be operated in an auto-fluorescence neglectable way [19]. This broadens the avenue to arrive at better medical bio-imaging with high signal-to-noise ratio and super imaging sensitivity [20].

Compared with the many studies on afterglow phosphors with an emission wavelength between 450 nm and 750 nm [9], there are much less studies that focus on the thermally stimulated SWIR luminescence. Properties of several typical infrared afterglow phosphors are summarized in Table 1. Only a few reports show the infrared afterglow decay in absolute radiance unit [19] like $mW.sr^{-1}.m^{-2}$ and the charge carrier trapping processes are often unclear. The proposed electron release processes and duration time as provided in Table 1 then should be regarded as indicative. It turns out that a trial and error approach appears to be often applied to discover a new SWIR afterglow phosphor, and the real nature of carrier trapping processes is usually not carefully identified such as in Table 1. There is a strong wish in the rational design of SWIR afterglow between ~900–1700 nm [7].

Methods to derive the locations of divalent and trivalent lanthanides energy levels within the band gap of inorganic crystals have now been constructed [21,22]. Using spectroscopic data, one can construct a so-called vacuum referred binding energy (VRBE) diagram [23]. Knowledge regarding the VRBE in defect levels, such as lanthanides, conduction band (CB), or valence band (VB), then provides a powerful tool to predict luminescence and to engineer carrier transport properties [24]. Note that the VRBE-guided method is mainly used to explore visible persistent phosphors [7] and systemic exploration of SWIR afterglow phosphors based on VRBE-guided conduction band or valence band engineering is still lacking. Particularly, to the best of our knowledge, there is no report on the design of SWIR afterglow based on hole release and tailored hole trapping depth via valence band engineering.

In this work, guided by a vacuum referred binding energy (VRBE) diagram, we will demonstrate how to design thermally stimulated Nd^{3+} infrared luminescence between ~900–1700 nm by a new combination of efficient energy transfer from Bi^{3+} to Nd^{3+} and adjustable hole trap depth via valence band engineering in the model La-, Gd-, Y-, and $LuPO_4$ compounds. Here, the thermally stimulated Nd^{3+} SWIR emission is obtained by means of hole release rather than the more commonly reported electron release.

Fig. 1 shows the VRBE diagram for YPO_4 with energy level locations of Bi^{2+}, Bi^{3+}, and lanthanides. Here, Tb^{3+}, Pr^{3+}, and Bi^{3+} act as ~1.45 eV, ~1.41 eV, and ~1.42 eV deep hole traps and Nd^{3+} as a ~0.96 eV deep electron trap as evidenced in previous experimental work [34,35]. The Bi^{3+} is predicted to act as a ~2.7 eV deep electron trap based on the VRBE diagram prediction.

Upon charging by β- or γ-ray irradiation, free charge carriers are created that can migrate via the valence band or conduction band. The electrons can be captured in a Bi^{3+}, or Nd^{3+} electron trap centre forming Bi^{2+}, or Nd^{2+} (arrows 1), and the holes can be captured by Bi^{3+}, Tb^{3+}, or Pr^{3+} generating Bi^{4+}, Tb^{4+}, or Pr^{4+} in their ground states (arrows 2) in YPO_4. Because the trap depth of the 2.7 eV deep

Table 1
Carrier trapping processes, emission, and afterglow durations for typical infrared afterglow phosphors. The symbol $\leftarrow e^-$ denotes that electrons liberate at a lower temperature than holes.

Compound	h^+	transport	e^-	peak (nm)	duration (h)	Refs.
$Zn_3Ga_2Ge_2O_{10}$	Cr^{3+}	$\leftarrow e^-$	host defect	696	360	[25]
$ZnGa_2O_4$	Cr^{3+}	$\leftarrow e^-$	host defect	687	5	[9]
$LiGa_5O_8$	Cr^{3+}	$\leftarrow e^-$	host defect	716	1000	[26]
$Zn_3Ga_2SnO_8$	Cr^{3+}	$\leftarrow e^-$	host defect	713	300	[27]
$MgGeO_3$	Yb^{3+}	$\leftarrow e^-$	host defect	1019	100	[28]
$Zn_3Ga_2Ge_2O_{10}$	Ni^{2+}	$\leftarrow e^-$	host defect	1290	12	[20]
$SrAl_2O_4$	Eu^{2+}	$\leftarrow e^-$	Dy^{3+}	1530 (Er^{3+})	0.2	[29]
$Y_3Al_2Ga_3O_{12}$	Ce^{3+}	$\leftarrow e^-$	Cr^{3+}	1532 (Er^{3+})	10	[30]
Ca_2SnO_4	Yb^{3+}	$\leftarrow e^-$	host defect	1000	10	[31]
$MgGeO_3$	Pr^{3+}	$\leftarrow e^-$	host defect	1085	120	[32]
$CdSiO_3$	Pr^{3+}	$\leftarrow e^-$	host defect	1085	120	[32]
$LaAlO_3$	Cr^{3+}	$\leftarrow e^-$	Sm^{3+}	986 (Er^{3+})	1	[19]
$Y_3Al_2Ga_3O_{12}$	Ce^{3+}	$\leftarrow e^-$	Cr^{3+}	1064 (Nd^{3+})	10	[33]

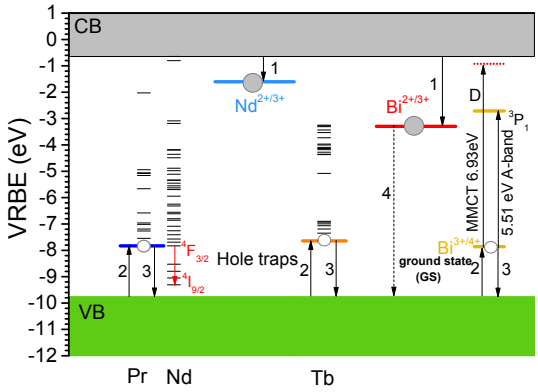

Fig. 1. Vacuum referred binding energy (VRBE) diagram of YPO_4 including the energy level locations for the ground states of Nd^{2+}, Pr^{3+}, Tb^{3+}, Bi^{2+}, and Bi^{3+}. The open circles represent holes and the filled circles are electrons. The charge carrier trapping processes indicated using numbered arrows are discussed in the text.

Bi^{3+} electron trapping centre is ~1.25 eV deeper than that of the ~1.45 eV deep hole trapping centres of Bi^{3+}, Tb^{3+}, or Pr^{3+}, the hole capturing centres will liberate holes (arrow 3) to combine with electrons at Bi^{2+} yielding Bi^{3+} A-band emission. If there is an efficient energy transfer process from Bi^{3+} to Nd^{3+}, then thermally stimulated Nd^{3+} SWIR luminescence near 1.06 μm can appear. The engineering of the hole trap depth of Tb^{3+} or Pr^{3+} hole trapping centres was demonstrated in $Y_{1-x}Lu_xPO_4$ solid solutions. By increasing x, the valence band (VB) energy can be tailored. The temperature when thermally stimulated Nd^{3+} ~1.06 μm luminescence appears can then be engineered by adjusting the Tb^{3+} or Pr^{3+} hole trap depth in $Y_{1-x}Lu_xPO_4$. We will verify all the above type of expectations, and provide a general VRBE-guided route to the rational design of thermally stimulated SWIR phosphors that can be applied to other inorganic compounds like $La_{1-x}Gd_xPO_4$ and $Gd_{1-x}La_xAlO_3$ solid solutions.

2. Experimental

All starting reagents were bought from Sigma-Aldrich and employed

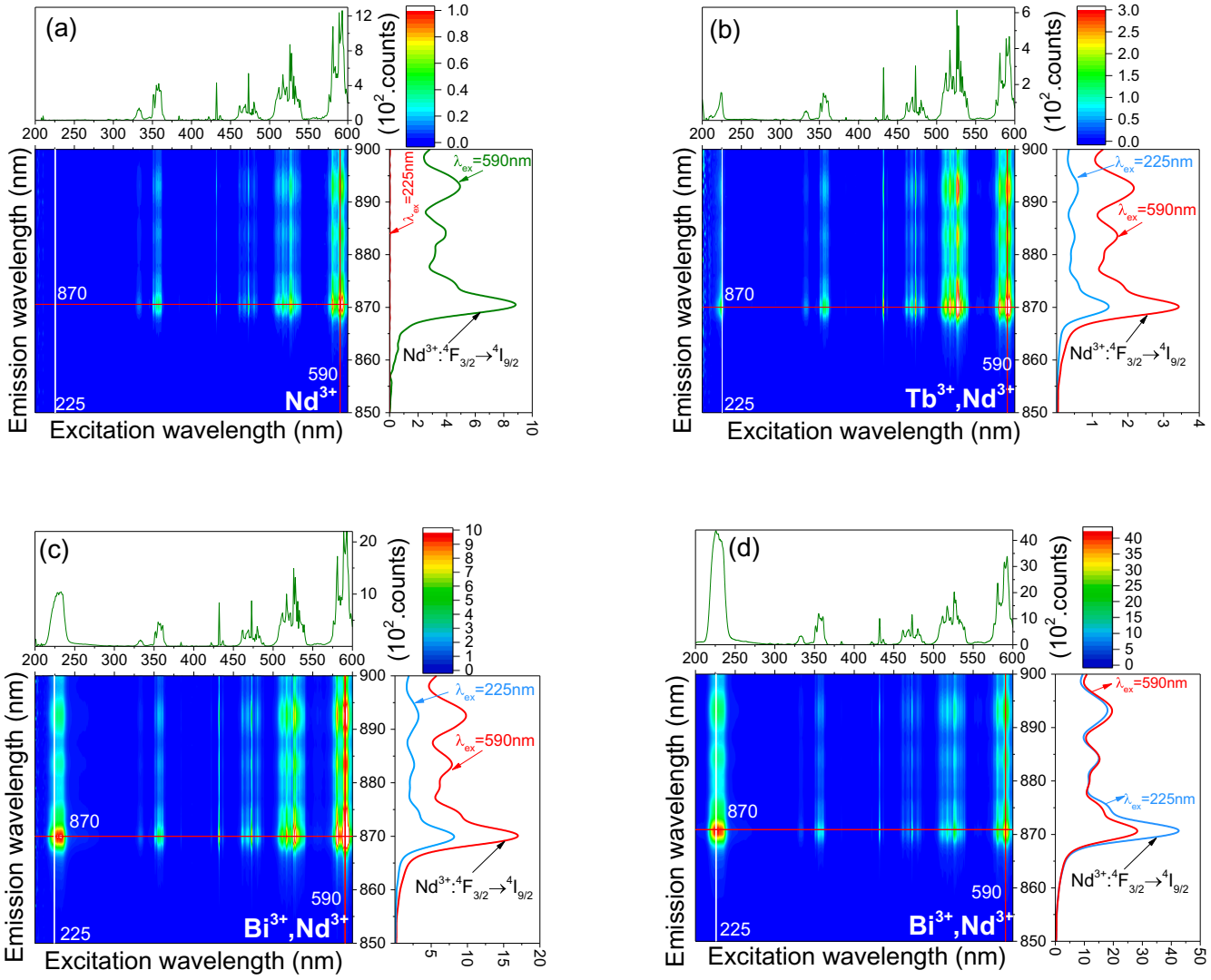

Fig. 2. Excitation-emission wavelength contour plots for (a) YPO_4:0.005Nd^{3+}, (b) YPO_4:0.005Tb^{3+}, 0.005Nd^{3+}, (c) YPO_4:0.005Bi^{3+}, 0.005Nd^{3+}, and (d) YPO_4:0.005Bi^{3+}, 0.02Nd^{3+}. The photoluminescence spectra under OPO laser excitation were recorded using a Si-based detector QE65000. A filter 10CGA-610 was used to select the Nd^{3+} emission above 610 nm. All the PL spectra were corrected by both the changes of laser intensity and the wavelength dependent quantum efficiency of the QE65000 detector.

without further treatments. Chemical reagents Bi_2O_3 (99.999%), $NH_4H_2PO_4$ (99.99%), and rare earth oxides (99.999%) were utilized as starting raw materials. Samples were synthesized by high-temperature solid-state reactions. Stoichiometric mixtures were thoroughly mixed in acetone. The mixtures were fired at 400 °C for 5 h and then at 1400 °C for 10 h in a covered corundum crucible in ambient atmosphere. The heating rate for the furnace is 3 °C per minute. After cooling, the as-synthesized compounds were ground well before further measurements. Solid solutions $Y_{1-x}Lu_xPO_4$:0.005Bi^{3+}, 0.005Ln^{3+}, 0.005Nd^{3+} (Ln^{3+} = Tb, and Pr) were prepared for x ranging from 0 to 1. The phase purities of all the

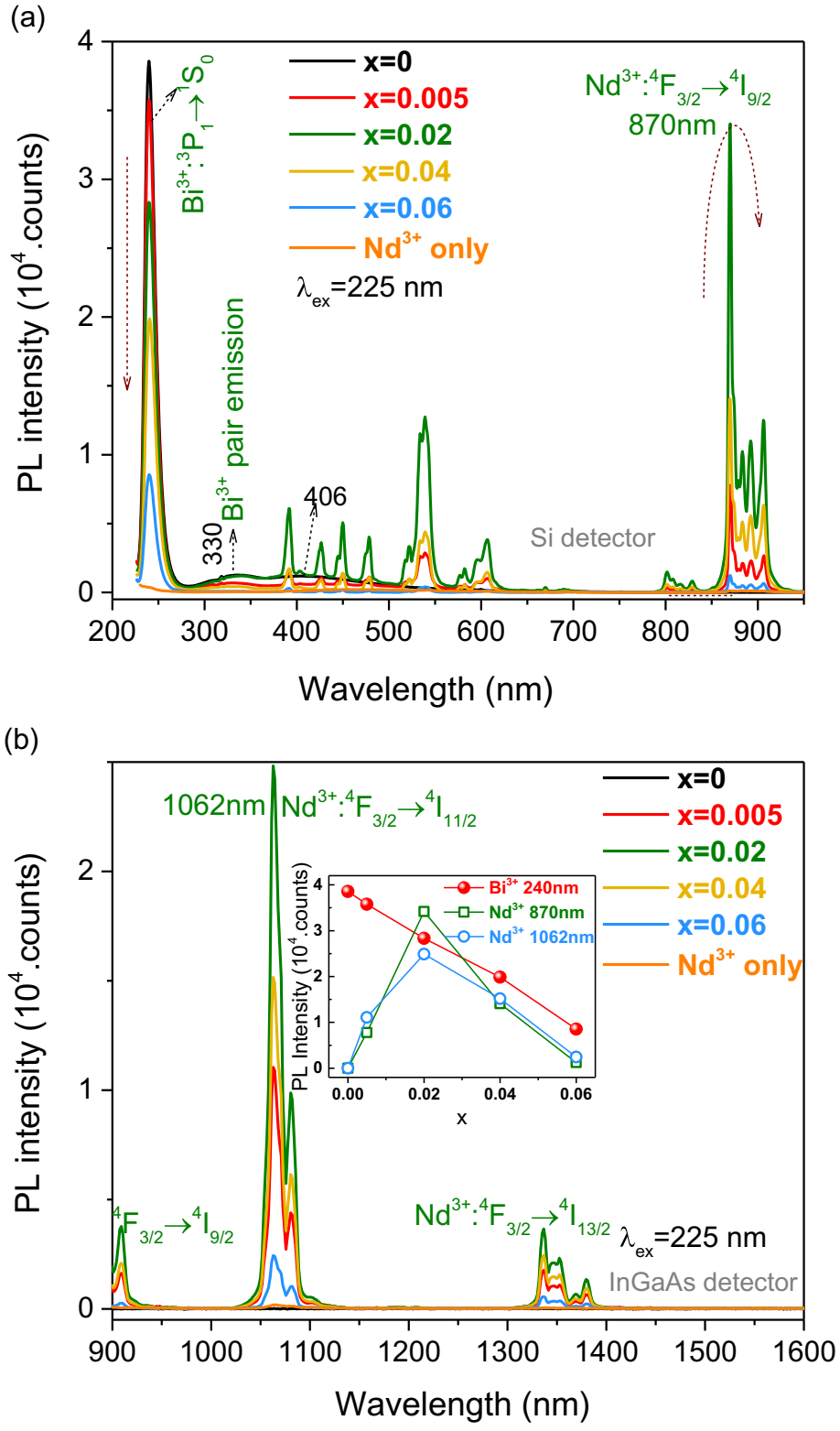

Fig. 3. 225 nm OPO laser excited photoluminescence (PL) spectra of YPO_4:0.005Bi^{3+}, xNd^{3+} (x = 0–0.06) and YPO_4:0.005Nd^{3+} crystals, a) between 225 and 975 nm recorded by a Si-based QE65000 detector, and b) between 900 and 1600 nm recorded using a InGaAs infrared detector NIRQ512. The inset in b) shows the variation of PL intensities of Bi^{3+} at 240 nm, Nd^{3+} at 870 and 1062 nm with increasing x.

samples were checked using a PANalytical XPert PRO x-ray diffraction system equipped with a cobalt Kα (λ = 0.178901 nm) X-ray tube.

The photoluminescence (PL) emission and excitation spectra were recorded at room temperature (RT) using a setup that consists of a UV/VIS spectrometer (Ocean Optics, QE65000), a near-infrared (NIR) spectrometer (Ocean Optics, NIRQ512), and a diode-pumped YAG:Nd laser system (NT230-100-SH/DUV-SCU). With an optical parametric oscillator (OPO), the output laser wavelength of a NT230-100-SH/DUV-SCU laser system can be tuned from 192 to 2600 nm. We used a Si-based detector QE65000 with a spectral range of 200–975 nm and an InGaAs based detector NIRQ512 with a spectral range of 900–1700 nm. The fluorescence lifetime curves were measured with a setup that includes a PerkinElmer MP-1913 photomultiplier (PMT), a UV/vis branch, a digitizer module, and an NT230-100-SH/DUV-SCU laser system. For these spectral measurements, all powder samples with different chemical composition were pressed into pills with 0.4 cm diameter and mass < 20 mg.

Thermoluminescence (TL) glow curves above room temperature

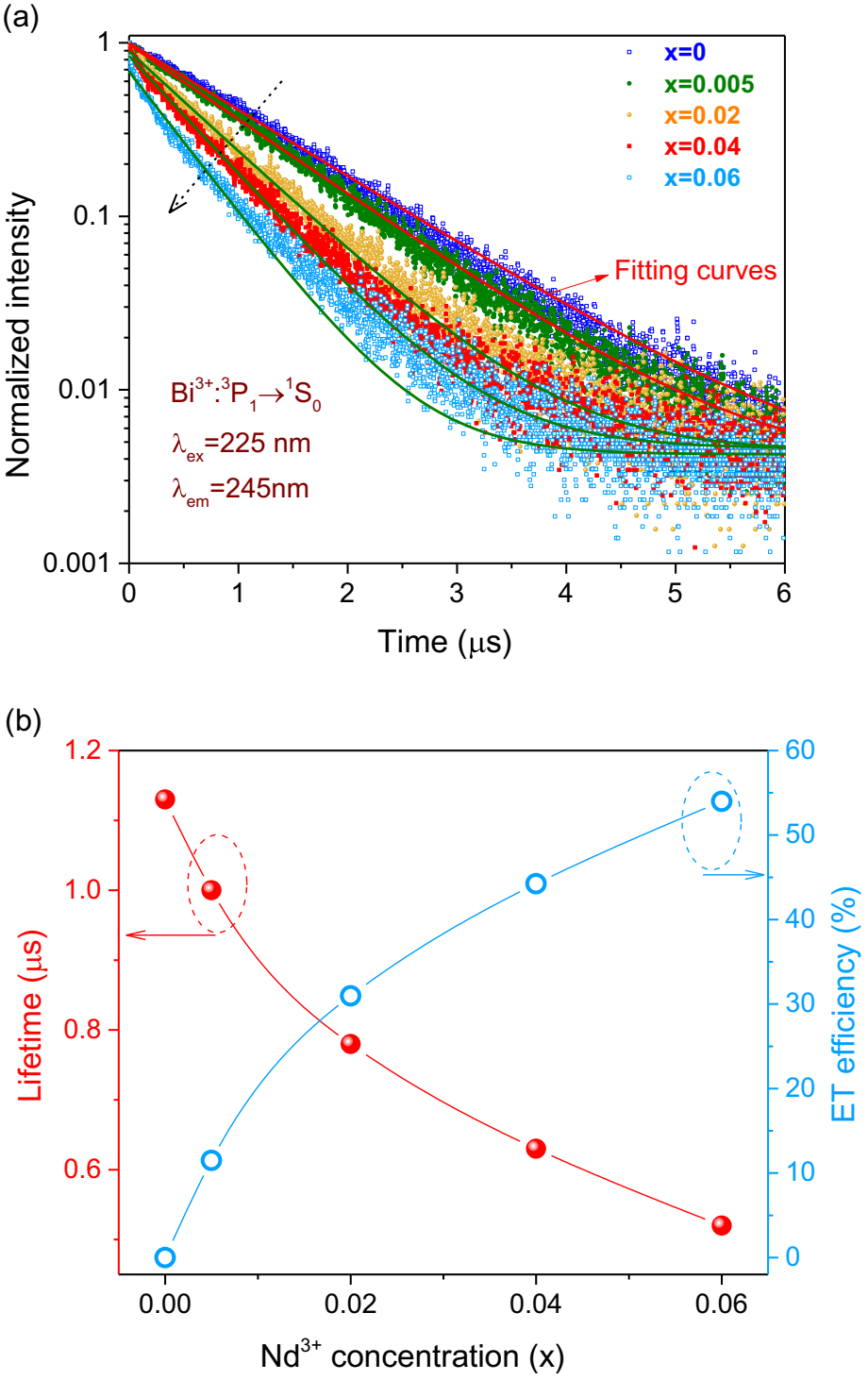

Fig. 4. (a) Fluorescence decay curves and (b) lifetime of Bi^{3+} A-band emission ($^3P_1 \rightarrow {}^1S_0$) at 245 nm upon 225 nm excitation as a function of Nd^{3+} concentration (x) in YPO_4:0.005Bi^{3+}, xNd^{3+} (x = 0–0.06) recorded at room temperature. The Nd^{3+} concentration dependence of the energy transfer efficiency of $Bi^{3+} \rightarrow Nd^{3+}$ in YPO_4:0.005Bi^{3+}, xNd^{3+} is shown.

(300–720 K) were recorded with a setup that consists of a RISØ TL/OSL reader (model DA-15), a controller (DA-20), and an EMI9635QA photomultiplier [36]. Prior to the TL measurements, all the samples were heated to 720 K 3 times to empty all relevant traps in complete darkness under a flow of N_2 gas and then cooled to room temperature followed by a β irradiation charging treatment using a $^{90}Sr/^{90}Y$ β source at a dose rate of 0.7 mGy/s. For the TL recording on samples where Bi^{3+} was the recombination centre, a 239 nm bandpass (239FS10-50, Andover Corporation) filter was placed between the PMT tube and the sample during the measurements.

Low-temperature thermoluminescence (LTTL) glow curves (90–450 K) were performed using a setup that consists of a $^{90}Sr/^{90}Y$ β irradiation source, a PerkinElmer channel photomultiplier tube (MP-1393), and a sample chamber that can be cooled to 90 K using liquid nitrogen under vacuum. Prior to the LTTL measurements, all the samples were heated to 450 K to empty all relevant traps and then charged at 90 K using β irradiation for 10 min at a dose rate of ~0.4 mGy/s. For $LaPO_4$:0.002Bi^{3+}, 0.005Pr^{3+}, 0.005Nd^{3+} a 600 nm bandpass (600FS40-50) filter was used to select Pr^{3+} emission, and for $LaPO_4$:0.002Bi^{3+}, 0.005Tb^{3+}, 0.005Nd^{3+}, a 545 nm bandpass (545FS40-50) filter was used to monitor Tb^{3+} emission.

Thermoluminescence emission spectra (TLEM) were recorded at a heating rate of 1 K/s by using the RISØ TL/OSL reader equipped with a UV/vis QE65000 spectrometer and a near infrared NIR512 spectrometer. All samples were first heated to 720 K to empty relevant traps and then charged at room temperature using γ-ray irradiation from a ^{60}Co source. The TLEM measured by QE65000 was corrected by the wavelength dependent quantum efficiency of the QE65000 spectrometer. A correction for the TLEM recorded by the infrared NIR512 spectrometer was not made.

3. Results

3.1. Photoluminescence spectroscopy

Fig. 2a)–c) shows the excitation-emission wavelength contour plots for YPO_4:0.005Nd^{3+}, YPO_4:0.005Tb^{3+}, 0.005Nd^{3+}, and YPO_4:0.005Bi^{3+}, 0.005Nd^{3+}. Characteristic Nd^{3+} 4f-4f excitation bands between 325 and 600 nm appear in YPO_4:0.005Nd^{3+} in Fig. 2a) while monitoring the 870 nm Nd^{3+} $^4F_{3/2} \rightarrow {}^4I_{9/2}$ emission. A weak additional excitation band near 225 nm appears in YPO_4:0.005Tb^{3+}, 0.005Nd^{3+} in Fig. 2b), which is assigned to the first Tb^{3+} 4f → 5d spin allowed transition. The same band is observed for Tb^{3+} singly doped YPO_4 when monitoring the Tb^{3+} emission at 545 nm as shown in Fig. S1. Much stronger and broader additional excitation band near 225 nm appears in YPO_4:0.005Bi^{3+}, 0.005Nd^{3+} in Fig. 2c) and YPO_4:0.005Bi^{3+}, 0.02Nd^{3+} in Fig. 2d), which is assigned to the Bi^{3+} $^1S_0 \rightarrow {}^3P_1$ excitation band. The same band appears in YPO_4:0.005Bi^{3+} in Fig. S3.

Fig. 3 shows the photoluminescence (PL) spectra of YPO_4:0.005Bi^{3+}, xNd^{3+} (x = 0–0.06) and YPO_4:0.005Nd^{3+} between 225 and 1600 nm recorded by Si and InGaAs detectors upon 225 nm excitation corresponding with the Bi^{3+} A-band wavelength. Like in YPO_4:Bi^{3+} in [37], the emission band near 240 nm is assigned to the Bi^{3+} $^3P_1 \rightarrow {}^1S_0$ A-band. The broad 368–600 nm emission band peaked near 406 nm is of unknown origin. The emission band centred near 330 nm is assigned to Bi^{4+}-Bi^{2+} pair emission [38]. With increasing x in YPO_4:0.005Bi^{3+}, xNd^{3+}, the photoluminescence intensity of the Bi^{3+} A-band at 240 nm continually decreases as shown in the inset of Fig. 3b), while both the PL intensities of Nd^{3+} at 870 nm and at 1062 nm first increase from x = 0 to x = 0.02, and then decrease with further increasing x due to the concentration quenching effect of Nd^{3+} emission [39].

Fig. 3 demonstrates efficient energy transfer from Bi^{3+} to Nd^{3+} and to further identify this energy transfer process, fluorescence decay measurements of Bi^{3+} $^3P_1 \rightarrow {}^1S_0$ emission at 245 nm were carried out for the YPO_4:0.005Bi^{3+}, xNd^{3+} (x = 0–0.06) samples as shown in Fig. 4a). All decay curves can be well fitted using the following single exponential formula plus a constant background intensity [40]:

$$I(t) = I_{b.g.} + I_0 \times \exp\left(-\frac{t}{\tau}\right) \quad (1)$$

where $I_{b.g.}$ is the background intensity, I_0 and I(t) stand for the Bi^{3+} $^3P_1 \rightarrow {}^1S_0$ emission intensities at time 0 and t, respectively. With Eq. (1) the lifetimes of the Bi^{3+} $^3P_1 \rightarrow {}^1S_0$ are determined and shown in Fig. 4b). The Bi^{3+} lifetime appears to decrease continually from 1.13 μs for x = 0 to 0.52 μs for x = 0.06 with increasing x, indicating an extra decay pathway because of a non-radiative energy transfer from the Bi^{3+} $^3P_1$ level to Nd^{3+}.

The lifetime τ or decay rate Γ for the excited $^3P_1$ state is related to the radiative decay rate, hereafter referred to as Γ_ν ($=\tau_\nu^{-1}$), and the non-radiative decay rate named as Γ_{nr} which consists of the non-radiative rates by multi-phonon relaxation (Γ_{phon}) to lower energy states and by an energy transfer process (Γ_{ET}) to Nd^{3+}. The following relation applies [19]

$$\Gamma_{tot} = \Gamma_\nu + \Gamma_{phon} + \Gamma_{ET} = \tau_{Bi,Nd}^{-1} \quad (2)$$

$$\eta_{ET} = \frac{\Gamma_{ET}}{\Gamma_\nu + \Gamma_{phon} + \Gamma_{ET}} = 1 - \frac{\tau_{Bi,Nd}}{\tau_{Bi}} \quad (3)$$

where Γ_{tot} represents the total decay rate, and τ_{Bi} and $\tau_{Bi,Nd}$ stand for the fluorescence lifetimes for the Bi^{3+} $^3P_1$ level in the Bi^{3+} singly and Bi^{3+}-Nd^{3+}-doped YPO_4. Using Eq. (3) the ET efficiencies η_{ET} from the Bi^{3+} $^3P_1$ level to Nd^{3+} are estimated and shown in Fig. 4b). The η_{ET} appears to increase with increasing x and arrives at 53.98% when x = 0.06.

3.2. Thermally stimulated luminescence

Fig. 5 presents the thermoluminescence glow curves of YPO_4:0.005Bi^{3+}, 0.005Nd^{3+}, and YPO_4:0.005Ln^{3+}, 0.005Nd^{3+} (Ln = Ce^{3+}, and Tb^{3+}) after charging with β irradiation. A TL glow peak near 350 K appears in all samples where the recombination emission is either from Bi^{3+} $^3P_1 \rightarrow {}^1S_0$, Ce^{3+} 5d → 4f, or Tb^{3+} 4f → 4f transitions. From the work by Bos *et al.* [41] on YPO_4:0.005Ce^{3+}, 0.005Nd^{3+} and YPO_4:0.005Tb^{3+}, 0.005Nd^{3+}, this 350 K glow peak was assigned to electron release from Nd^{2+} and recombination with the hole on Ce^{4+} or Tb^{4+}. Depending on analysis methods [2,42–45] a trapping depth E (eV) between 0.89 and 0.98 eV from this 350 K glow

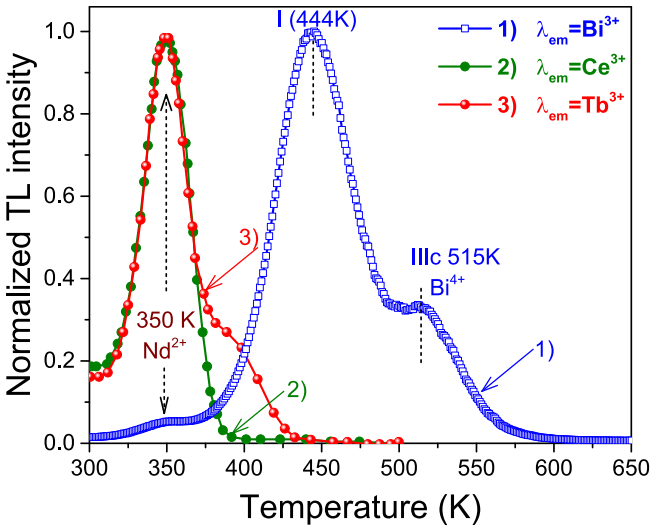

Fig. 5. Normalized TL glow curves for 1) YPO_4:0.005Bi^{3+}, 0.005Nd^{3+}, 2) YPO_4:0.005Ce^{3+}, 0.005Nd^{3+}, and 3) YPO_4:0.005Tb^{3+}, 0.005Nd^{3+} recorded at a heating rate of 5 K/s monitoring characteristic emission either from Bi^{3+}, Ce^{3+}, or Tb^{3+}. The data on YPO_4:0.005Ln^{3+}, Nd^{3+} (Ln = Ce^{3+}, and Tb^{3+}) crystals were derived from Bos *et al.* [41].

peak in YPO_4 was obtained [46] that agrees with the VRBE diagram. Compared with the experimental ~1.42 eV Bi^{3+} hole trap depth found in ref. [35], the electrons trapped at Nd^{2+} liberate at a lower temperature than the holes trapped at Bi^{4+}. They will recombine with the holes on Bi^{4+} to give the TL glow near 350 K with typical Bi^{3+} A-band emission in YPO_4:0.005Bi^{3+}, 0.005Nd^{3+}.

Thermoluminescence emission (TLEM) spectra were recorded for YPO_4:0.005Nd^{3+}, YPO_4:0.005Bi^{3+}, 0.005Nd^{3+}, and YPO_4:0.005Tb^{3+}, 0.005Nd^{3+} in order to clarify the role of Nd^{3+} as a 1.06 μm emitting centre during the TL readout. No TL glow peaks with typical Nd^{3+} luminescence between 200 and 1700 nm were observed for YPO_4:0.005Nd^{3+}. Fig. 6a) shows the TL emission spectrum for YPO_4:0.005Bi^{3+}, 0.005Nd^{3+} recorded by a Si spectrometer. Not only characteristic Bi^{3+} A-band but also Nd^{3+} $^4F_{3/2} \rightarrow {}^4I_{9/2}$ emission near 870 nm appears when co-doping Bi^{3+} in YPO_4:0.005Nd^{3+}. From the study in ref. [35] for YPO_4:0.005Bi^{3+}, the TL glow peaks IIIc and I that are also present in Fig. 5 were attributed to hole release from Bi^{4+} and from a host-related hole trapping centre respectively. The holes recombine with the electrons captured at Bi^{2+} to generate Bi^{3+} A-band emission. Fig. 6b) shows the TLEM spectrum of YPO_4:0.005Bi^{3+}, 0.005Nd^{3+} recorded by an InGaAs detector in the wavelength range from 900 to 1700 nm. Thermally stimulated Nd^{3+} $^4F_{3/2} \rightarrow {}^4I_{11/2}$ emission near 1.06 μm emerges. The TL glow peaks I and IIIc when monitoring the Bi^{3+} A-band emission or when monitoring the Nd^{3+} 4f-4f emission near 870 nm and 1.06 μm appear to have the same shape. The cut-off of black body radiation above 1650 nm in Fig. 6b) is an artefact because intensity was not corrected for the wavelength dependent quantum efficiency of the InGaAs NIR512 detector.

Fig. 6c) and d) show the TL emission spectra for YPO_4:0.005Tb^{3+}, 0.005Nd^{3+} in the wavelength region from 200 to 1700 nm. Characteristic Tb^{3+} $^5D_4 \rightarrow {}^7F_5$ emission at 545 nm with associated TL glow band near 350 K appears in Fig. 6c), which is 300 times weaker than Bi^{3+} A-band emission in YPO_4:0.005Bi^{3+}, 0.005Nd^{3+} in Fig. 6a). Note that the characteristic Nd^{3+} 4f-4f emission near 870 nm and 1.06 μm does not appear in YPO_4:0.005Tb^{3+}, 0.005Nd^{3+}.

Fig. 6a) shows that the Bi^{3+} A-band emission of the Bi^{4+} hole release glow peak IIIc is about 7 times weaker than that of the intrinsic defect hole release glow peak I in YPO_4:0.005Bi^{3+}, 0.005Nd^{3+}. The VRBE diagram of YPO_4 in Fig. 1 shows that Bi^{3+}, Tb^{3+}, and Pr^{3+} have almost the same ~1.42 eV hole trap depth. Their hole trapping capacity, however, may be different. We, therefore, combined Tb^{3+} or Pr^{3+} as a shallow hole trapping centre with Bi^{3+} and Nd^{3+} into YPO_4 to

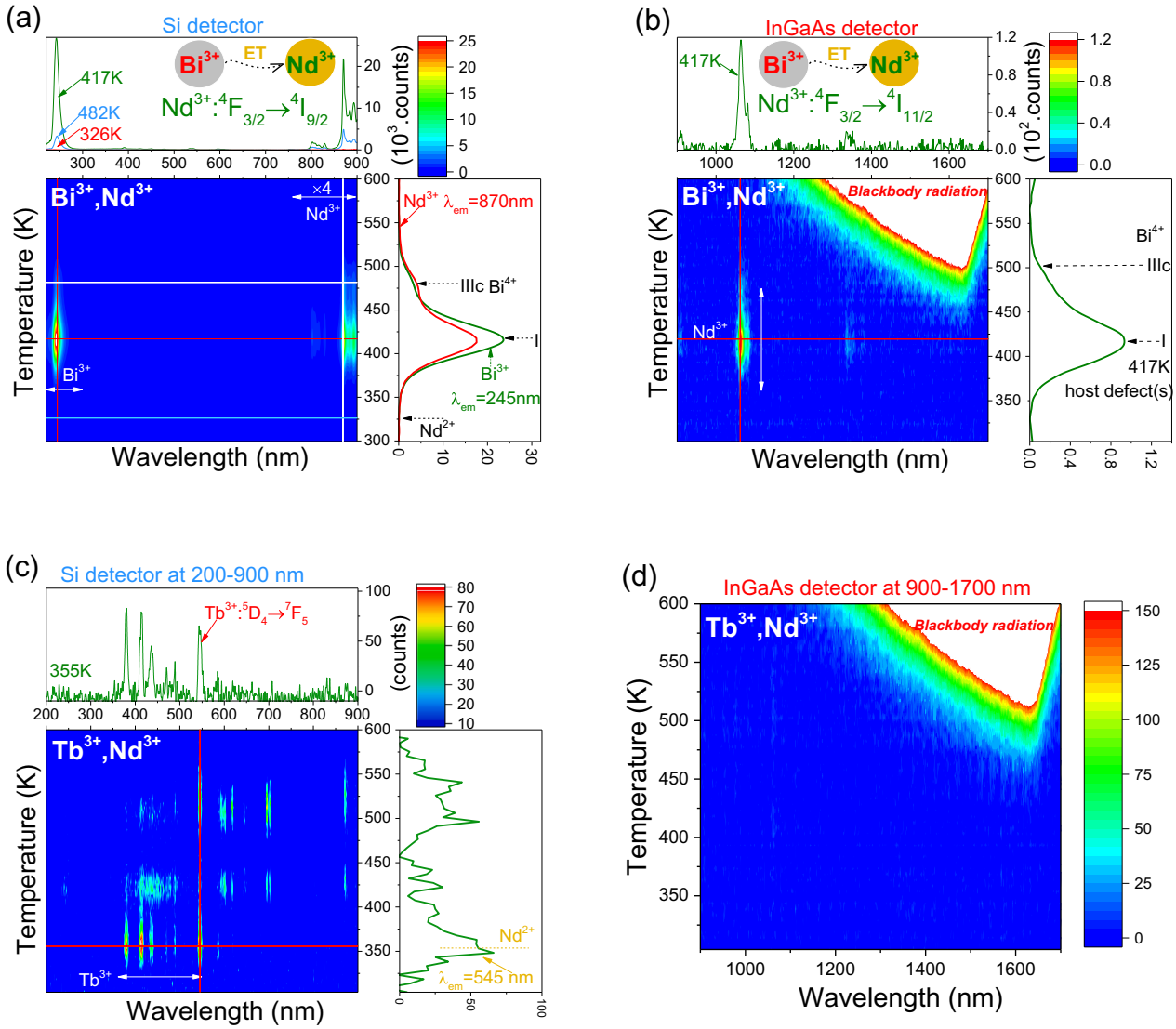

Fig. 6. Thermoluminescence emission (TLEM) plots for (a),(b) YPO_4:0.005Bi^{3+}, 0.005Nd^{3+} and (c),(d) YPO_4:0.005Tb^{3+}, 0.005Nd^{3+} recorded at a heating rate of 1 K/s after γ-ray irradiation from a ^{60}Co source. The emission signal from each sample has been measured using a Si detector QE65000 at 200–900 nm and an InGaAs detector at 900–1700 nm.

explore thermally stimulated luminescence of Nd^{3+} near 1.06 μm for the second bio-imaging window. Fig. 7a) shows the TLEM spectrum for YPO_4:0.005Bi^{3+}, 0.005Tb^{3+}, 0.005Nd^{3+} after γ-ray irradiation and recorded by a Si detector in the wavelength region from 200 to 925 nm. Characteristic Bi^{3+} A-band, Tb^{3+} 4f-4f, and Nd^{3+} $^4F_{3/2} \rightarrow {}^4I_{9/2}$ emission near 870 nm all appear. From previous study on YPO_4:0.005Bi^{3+}, 0.005Tb^{3+} (Fig. S3c) in ref. [35], the TL glow peak IIIa monitoring the Bi^{3+} A-band emission was attributed to hole liberation from Tb^{4+} and recombination with an electron captured at Bi^{2+}. The simultaneous appearance of Tb^{3+} 4f-4f emission was attributed to the energy transfer from Bi^{3+} to Tb^{3+} [37]. Fig. 7b) is the TLEM plot for YPO_4:0.005Bi^{3+}, 0.005Tb^{3+}, 0.005Nd^{3+} recorded by an InGaAs spectrometer between

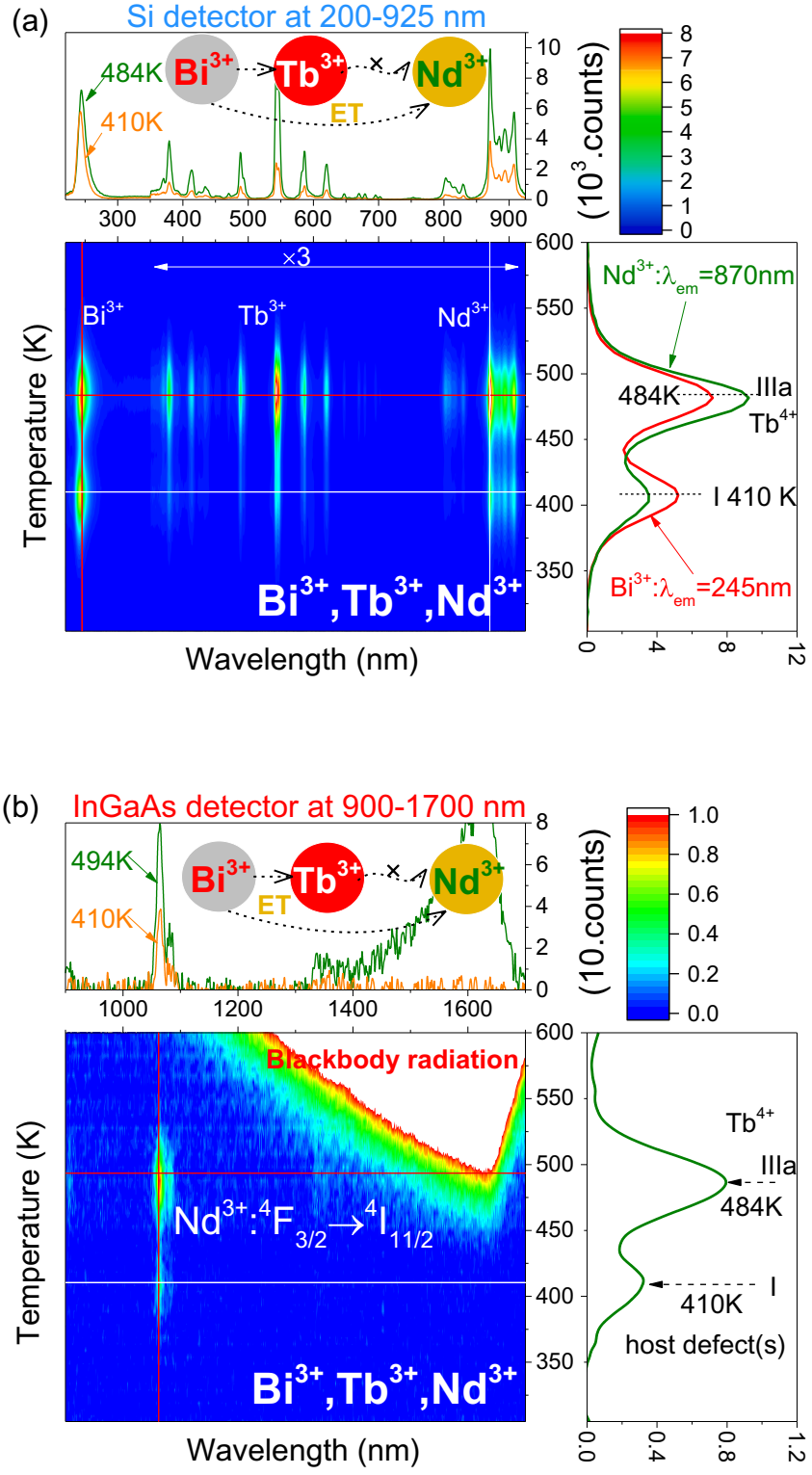

Fig. 7. TL emission (TLEM) spectra for a YPO_4:0.005Bi^{3+}, 0.005Tb^{3+}, 0.005Nd^{3+} sample recorded using (a) a Si detector at 200–925 nm and (b) an InGaAs detector at 900–1700 nm at a heating rate of 1 K/s after γ-ray irradiation.

900 and 1700 nm. Thermally stimulated Nd^{3+} emission near 1.06 μm appears, and the TL glow peak IIIa near 484 K when monitoring the Bi^{3+} A-band emission at 245 nm, or when monitoring Nd^{3+} emission at 1.06 μm or at 870 nm shares the same shape.

4. Discussion

We will first deal with the energy transfer (ET) process from Bi^{3+} to Nd^{3+} in YPO_4. Then, a new combination of that efficient energy transfer from Bi^{3+} to Nd^{3+} and using adjustable hole trap depth by valence band engineering guided by vacuum referred binding energy diagram is presented to the rational design of thermally stimulated Nd^{3+} infrared emission near ~1.06 μm.

4.1. 1.06 μm Nd^{3+} emission via energy transfer from Bi^{3+} or Tb^{3+}

Fig. 8 shows the energy level diagram for Bi^{3+}, Nd^{3+}, and Tb^{3+} in YPO_4. The excited $^3P_1$ state of Bi^{3+} is energetically close to the Nd^{3+} $^2F2_{7/2}$ and $^2F2_{5/2}$ levels, indicating that an energy transfer process from Bi^{3+} to Nd^{3+} is energetically possible. The excited Nd^{3+} $^2F2_{7/2}$ and $^2F2_{5/2}$ levels can relax to $^4F_{3/2}$ level through non-radiative relaxation to yield Nd^{3+} $^4F_{3/2} \rightarrow {}^4I_j$ (j = 9/2, 11/2, and 13/2) infrared emission near 870 nm, 1062 nm, and 1337 nm respectively. This is observed in Fig. 2c) where the characteristic Bi^{3+} A-band ($^1S_0 \rightarrow {}^3P_1$) in the photoluminescence excitation spectrum of Bi^{3+}-Nd^{3+}-codoped YPO_4 appears when monitoring Nd^{3+} emission. This Bi^{3+} A-band increases 3 times with increasing Nd^{3+} concentration in Fig. 2d), revealing that a more efficient energy transfer process from Bi^{3+} to Nd^{3+} occurs in YPO_4:0.005Bi^{3+}, 0.02Nd^{3+}. The same energy transfer is demonstrated in Fig. 3 and quantified further in Fig. 4.

Fig. 8 also shows that the first spin allowed Tb^{3+} $4f^75d$ excited state is not resonant with Nd^{3+} excited states. The Tb^{3+} ions in that 5d state can relax very rapidly via non-radiative relaxation to the $^5D_3$, $^5D_4$ levels or high spin [HS] $4f^75d$ near 37300 cm^{-1} [48] which are energetically close to Nd^{3+} levels, suggesting the possibility of energy transfer from Tb^{3+} $^5D_3$, $^5D_4$ or spin-forbidden $4f^75d$ levels to Nd^{3+} levels like $^4G_{7/2}$. If energy transfer from Tb^{3+} to Nd^{3+} is present, then a Tb^{3+} 4f-5d excitation band is expected in the PL excitation spectrum of Tb^{3+}-Nd^{3+}-codoped YPO_4 when monitoring Nd^{3+} emission. Fig. 2b) shows that a weak Tb^{3+} 4f-5d excitation band near 225 nm indeed appears in YPO_4:0.005Tb^{3+}, 0.005Nd^{3+} while monitoring the Nd^{3+} 870 nm emission. Considering that the additional excitation band near 225 nm induced by Tb^{3+} co-doping is much smaller than the one by Bi^{3+} co-doping in YPO_4:0.005Nd^{3+}, the energy transfer efficiency of $Bi^{3+} \rightarrow Nd^{3+}$ in YPO_4:0.005Bi^{3+}, 0.005Nd^{3+} appears to be much higher than that of $Tb^{3+} \rightarrow Nd^{3+}$ in YPO_4:0.005Tb^{3+}, 0.005Nd^{3+}.

4.2. Tuneable thermally stimulated luminescence of Nd^{3+} near 1.06 μm by engineering hole trap depths of Tb^{3+} and Pr^{3+} in $Y_{1-x}Lu_xPO_4$ and $La_{1-x}Gd_xPO_4$

Fig. 9a) shows that the vacuum referred binding energy (VRBE) in the $^2P_{1/2}$ ground state of Bi^{2+} is near −3.3 eV and the VRBE in the Bi^{3+} $^1S_0$, Tb^{3+} and Pr^{3+} $4f^n$ ground states are near −7.8 eV in the La-, Y-, and $LuPO_4$ compounds. Bi^{3+} will act as an about 2.7 eV deep electron trapping centre, while Bi^{3+}, Tb^{3+}, and Pr^{3+} will act as hole trapping centres which hole trap depths depend on the VRBE at the valence band top. That valence band top rises by 0.85 eV in discrete steps from Lu-, to Y-, Gd-, and to $LaPO_4$. The hole trap depths and the temperature T_m for TL glow peaks due to hole release from Tb^{4+}, Pr^{4+}, or Bi^{4+} should decrease accordingly. We will focus on using Tb^{3+} and Pr^{3+} as tuneable hole traps to demonstrate the concept of deliberate design of persistent Nd^{3+} SWIR luminescence via valence band engineering.

First, we testified the adjustable thermally stimulated Nd^{3+} SWIR emission in $Y_{1-x}Lu_xPO_4$ solid solutions as shown in Fig. S4–6. Although we demonstrated that the temperature of hole release can be tuned, the T_m of the TL glow peaks from Tb^{4+} and Pr^{4+} are at a too high temperature of 500 K and shift the wrong direction. They need to be shifted close to 300 K in order to realize Nd^{3+} SWIR afterglow for applications.

Fig. 9a) shows that the VRBE at the valence band top of $LaPO_4$ is about 0.85 eV higher than that in $LuPO_4$ which implies that the TL glow peaks from Tb^{4+} and Pr^{4+} should move towards RT. Bi^{3+} and lanthanide-doped $LaPO_4$ phosphors were thus synthesized to explore Nd^{3+} SWIR afterglow at room temperature. Fig. S7a) shows a TL emission plot for $LaPO_4$:0.002Bi^{3+}, 0.005Pr^{3+}, 0.005Nd^{3+} after γ-ray irradiation. The TL glow peaks I and IIb when monitoring the Pr^{3+} 4f-4f emission or when monitoring the Nd^{3+} emission near 900 nm and 1.07 μm appear to share the same shape. Because glow peak IIb is near RT, Nd^{3+} SWIR afterglow appears in $LaPO_4$:0.002Bi^{3+}, 0.005Pr^{3+}, 0.005Nd^{3+} in Fig. S7b).

To identify the charge carrier trapping processes, Fig. 10a) shows the low-temperature TL glow curves for Bi^{3+} and lanthanides doped $LaPO_4$ by monitoring emission from Eu^{3+}, Pr^{3+}, or Tb^{3+}. Herein, Bi^{3+} and Eu^{3+} are predicted to act as ~2.81 and ~3.67 eV deep electron traps based on the VRBE diagram in Fig. 9a), while Tb^{3+} and Pr^{3+} act as 0.63 and 0.55 eV shallow hole trapping centres in $LaPO_4$ based on the previous experimental work in ref. [34]. By combining the deep electron trap Eu^{3+} with the shallow hole trap Tb^{3+} or Pr^{3+}, the holes trapped at Tb^{4+} or Pr^{4+} are liberated to recombine with the electrons at Eu^{2+} producing Eu^{3+} red emission [34] with TL peaks IIIa (Tb) near 240 K in Fig. 10a1) and IIIb (Pr) near 210 K in Fig. 10a3). The same glow peaks IIIa in Fig. 10a2) and IIIb in Fig. 10a4) indeed appear when Eu^{3+} is replaced by the 2.81 eV deep electron trap Bi^{3+}. Hole release from Tb^{4+} or Pr^{4+} like in Fig. 10a1) or 10a3) is also present in $LaPO_4$:0.002Bi^{3+}, 0.005Tb^{3+}, 0.005Nd^{3+} and $LaPO_4$:0.002Bi^{3+}, 0.005Pr^{3+}, 0.005Nd^{3+} in Fig. 10a2) and a4) where instead of at Eu the recombination is at Bi.

This again demonstrates that the temperature of hole release and related SWIR emission can be engineered. However, in $LaPO_4$ the glow peaks IIIa and IIIb are shifted too far and appear below room temperature. The TL glow peaks I and IIb with red Pr^{3+} emission in Fig. 10a4) cannot be attributed to electron release from host-related electron traps with recombination on Pr^{4+} because the holes trapped at Pr^{4+} have already disappeared as a result of recombination with the electrons at Bi^{2+} near 210 K. Therefore, they are attributed to hole release from unidentified defect centres in $LaPO_4$. The appearance of Pr^{3+}, Nd^{3+}, or Tb^{3+} emission in Fig. 10a4) and also Fig. S7a-8 is assigned to energy transfer from Bi^{3+}, which is similar as that in YPO_4 in Fig. 7 and other solid solutions $Y_{1-x}Lu_xPO_4$ in Fig. S5. Supporting

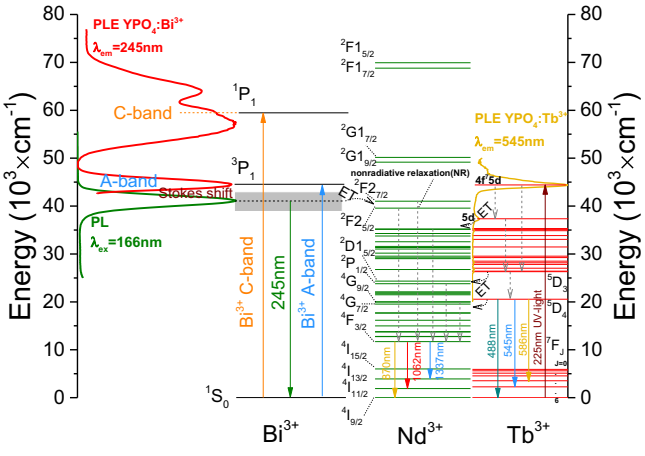

Fig. 8. Energy level diagrams of Bi^{3+}, Nd^{3+}, and Tb^{3+} in YPO_4. The possible energy transfer routes of $Bi^{3+} \rightarrow Nd^{3+}$ and $Tb^{3+} \rightarrow Nd^{3+}$ are indicated. The experimental energy levels for Nd^{3+} were derived from ref. [47], and for Tb^{3+} 5d and Bi^{3+}, the levels were derived from the experimental spectroscopy in this work.

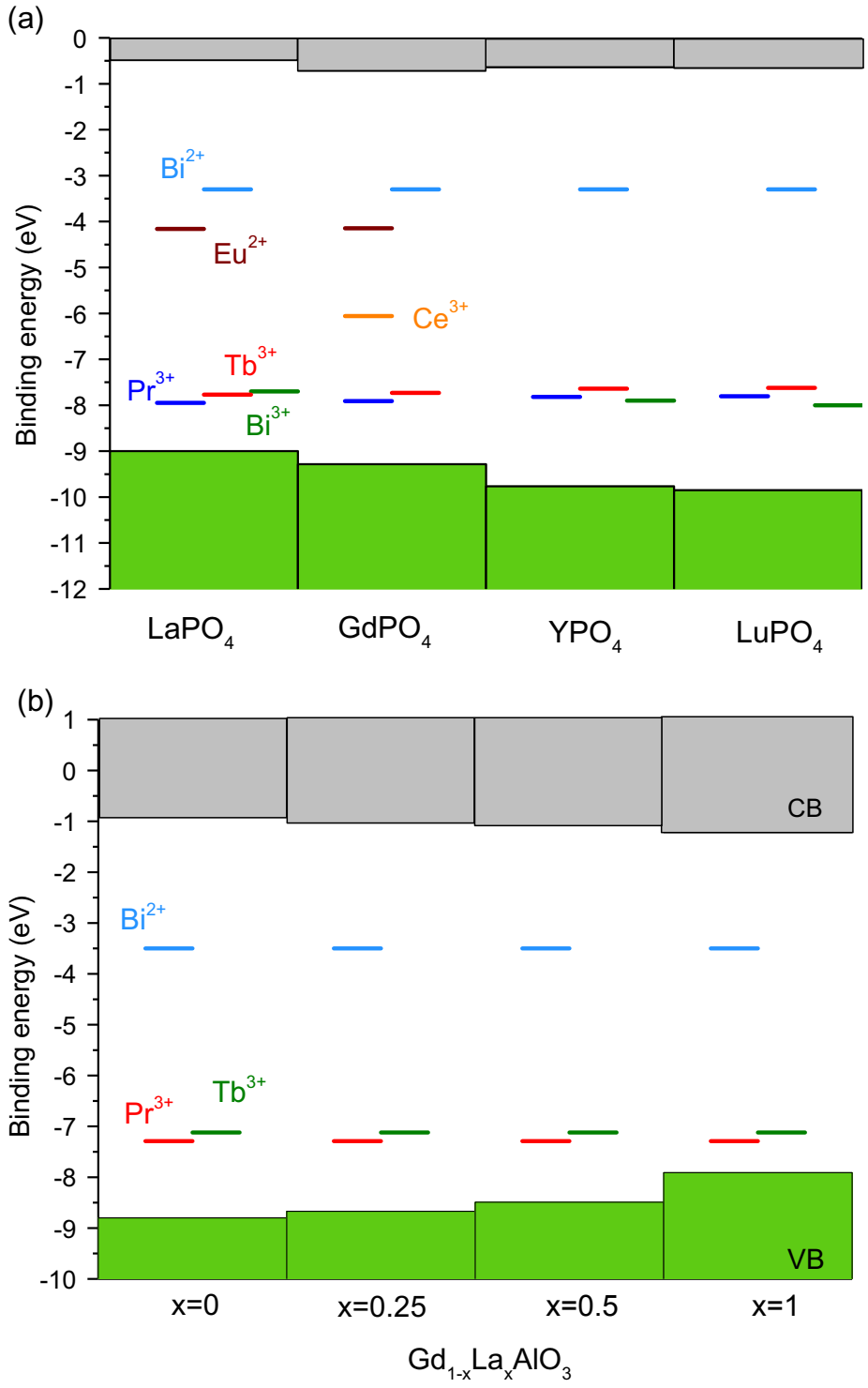

Fig. 9. Stacked VRBE diagrams for (a) $REPO_4$ and (b) $Gd_{1-x}La_xAlO_3$ solid solutions including the vacuum referred binding energy in the ground states of Pr^{3+}, Tb^{3+}, Ce^{3+}, Eu^{2+}, Bi^{3+}, and Bi^{2+}. The data on constructing the diagram (a) were obtained from ref. [34,35]. For diagram (b) the Tb^{3+} and Pr^{3+} levels were obtained from ref. [49] and the Bi^{2+} level near −3.5 eV for oxide compounds from ref. [50] was used.

evidence is the appearance of the same TL glow peaks I and IIb when monitoring the emission either from Pr^{3+} or Nd^{3+} in Fig. S7a) or from Tb^{3+} in Fig. S8. This is also supported by the spectral overlap of $LaPO_4$:0.002Bi^{3+} at 325–600 nm emission (Fig. S10) with the 4f-4f excitation bands of Tb^{3+} [51], Pr^{3+} [52], and Nd^{3+} like in Fig. 2a), which indicates the possibility of ET from Bi^{3+} to Tb^{3+}, Pr^{3+}, or Nd^{3+} in $LaPO_4$.

The method using $Bi^{3+} \rightarrow Nd^{3+}$ ET and engineering the hole trapping depths of Tb^{3+}, Pr^{3+}, or intrinsic hole trapping centres by valence band changing in the phosphate compounds can also be applied to solid solutions like $La_{1-x}Gd_xPO_4$ and $Gd_{1-x}La_xAlO_3$. Fig. 9a) demonstrates that the VRBE at the valence band top of $GdPO_4$ is about 0.3 eV lower than in $LaPO_4$ which indicates that the TL glow peaks IIIa near 240 K and IIIb near 210 K in Fig. 10a2) and a4) should move towards room temperature in $La_{1-x}Gd_xPO_4$ by increasing x.

To further demonstrate the design methodology of SWR afterglow

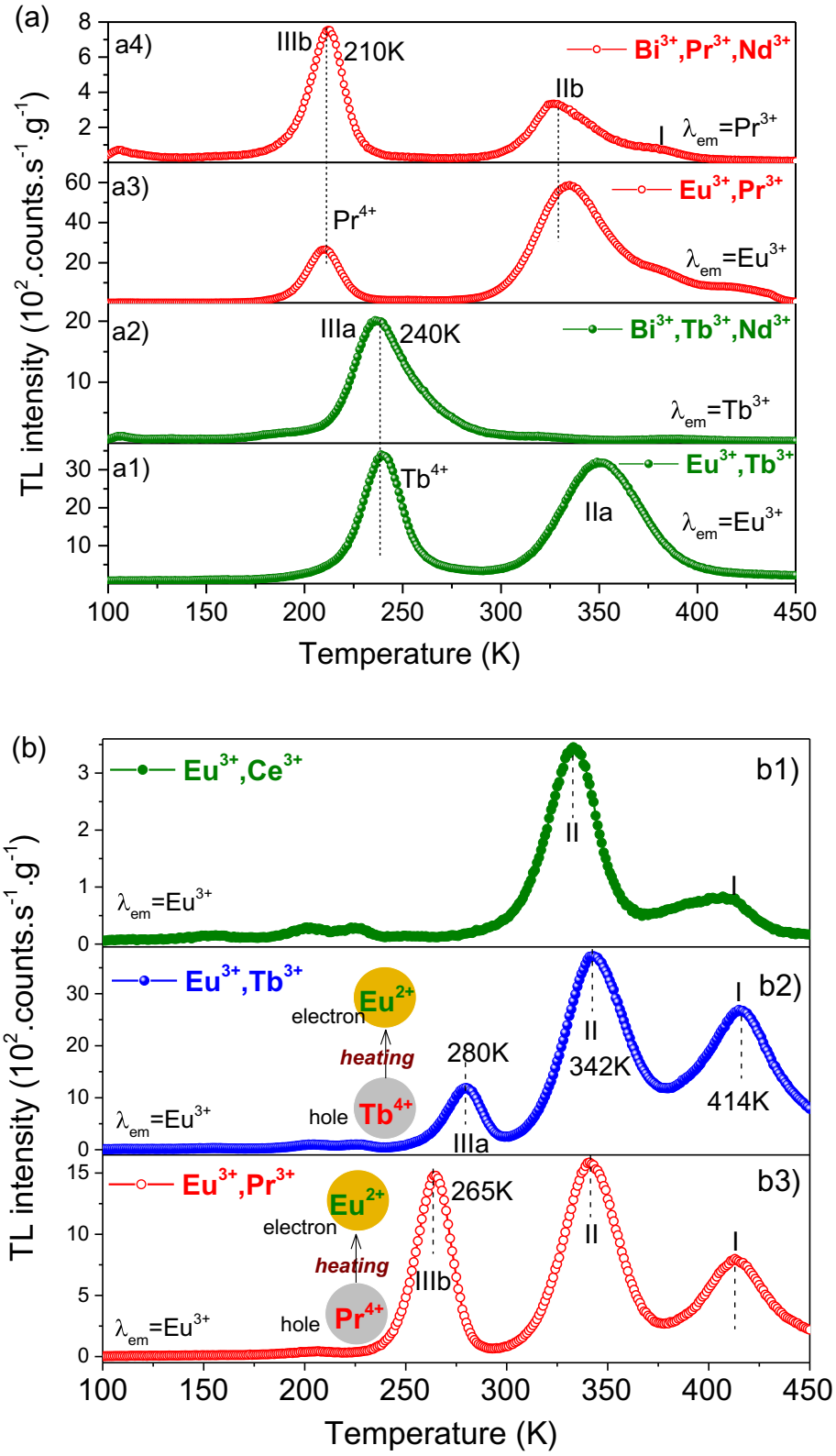

Fig. 10. Low-temperature TL glow curves for (a) Bi^{3+} and Ln^{3+} doped $LaPO_4$ and (b) $GdPO_4$:0.005Eu^{3+}, 0.005Ln^{3+} (Ln = Ce, Tb, and Pr) recorded at a heating rate of 1 K/s after 600 s β irradiation in the temperature range between 100 and 450 K. Eu^{3+} emission was monitored in a1)-a3) and b1-b3). The green Tb^{3+} and red Pr^{3+} emissions were respectively selected in a2) and a4). The TL intensities were corrected by sample mass and irradiation time. (For interpretation of the references to colour in this figure legend, the reader is referred to the web version of this article.)

phosphors in $La_{1-x}Gd_xPO_4$ solid solutions, the hole detrapping processes of Tb^{3+} and Pr^{3+} hole capturing centres are first studied in $GdPO_4$. Fig. 10b) shows the low-temperature TL glow curves for $GdPO_4$:0.005Eu^{3+}, 0.005Ln^{3+}. Compared with Ce^{3+} codoping in $GdPO_4$ in Fig. 10b1), Tb^{3+} gave rise to a new TL glow peak near 280 K named as IIIa in Fig. 10b2) and Pr^{3+} to a TL peak denoted as IIIb at

about 15 K lower temperature in Fig. 10b3). The TL glow peak I for $GdPO_4$:0.005Eu^{3+}, 0.005Tb^{3+} was further studied by a variable heating rate plot using RISØ TL/OSL reader in Fig. S12b). This provides a frequency factor of 1.07×10^{12} s^{-1}, which is assumed to apply to TL glow peaks IIIa and IIIb. Their trapping depths E (eV) are then determined by employing the temperature T_m at the maximum of the glow curve and solving the following first-order TL-recombination kinetics formula [44,45]:

$$\frac{\beta E}{kT_m^2} = s \times \exp\left(-\frac{E}{kT_m}\right) \quad (4)$$

where $\beta = 1$ K/s represents the heating rate, k denotes the Boltzmann constant (8.62×10^{-5} eV/K), and s is the frequency factor (1.07×10^{12} s^{-1}). With Eq. (4), the trap depths for IIIa and IIIb are respectively derived to be 0.72, and 0.68 eV.

The vacuum referred binding energy (VRBE) scheme for $GdPO_4$ in Fig. 9a) predicts that Eu^{3+} and Bi^{3+} act as ~3.43, and 2.78 eV deep electron traps, while Tb^{3+}, Pr^{3+}, and Ce^{3+} act as 1.56, 1.38, and 3.23 eV deep hole traps. When holes are produced in the valence band, they tend to be shared between two neighbouring oxygen anions to form a thermally activated V_k centre [53,54] located above the valence band top in a VRBE scheme [34,55]. Since La-, Gd-, YPO_4 are quite similar, the binding energy for a V_k centre in $GdPO_4$ is assumed to be about 0.6 eV, like in La-, and YPO_4 [34]. The effective hole trap depths of Tb^{3+}, Pr^{3+}, and Ce^{3+} are then determined to be 0.96, 0.78, and 2.63 eV, respectively. Using Eq. (4) with $\beta = 1$ K/s and the above predicted hole trap depths, one can estimate that the hole liberation from Tb^{4+}, Pr^{4+}, or Ce^{4+} in $GdPO_4$ gives TL glow peaks T_m near 369, 302, and 980 K, respectively. Obviously, the Ce^{4+} hole trap is far too deep to liberate a hole between 100 and 450 K. The estimated TL peaks T_m for hole liberation from Tb^{4+} and Pr^{4+} traps are in the measurement range, and we assign the TL glow peaks IIIa (0.72 eV) and IIIb (0.68 eV) to the hole liberation from Tb^{4+} in Fig. 10b2) and Pr^{4+} in Fig. 10b3). Considering that glow peaks I and II appear in all three samples, they are attributed hole liberation from intrinsic host defect(s) and recombination with the electrons trapped at Eu^{2+}.

Like $LaPO_4$ in Fig. 10a), Bi^{3+} and/or Ln^{3+} doped $La_{1-x}Gd_xPO_4$ solid solutions were further synthesized to explore the rational design of Nd^{3+} SWIR afterglow by using adjustable hole trap depth of Tb^{3+} and Pr^{3+}.

Fig. 11 shows the low-temperature TL glow curves for Bi^{3+} and/or Ln^{3+} doped $La_{1-x}Gd_xPO_4$ with x range from 0 to 1. For the samples each with the same Pr^{3+} hole trap but with different electron trap of Eu^{3+} in Fig. 11a1)–a3) and of Bi^{3+} in Fig. 11a4)–a6), the glow peak IIIb shares almost the same shape. It shifts from 210 K to 265 K with increasing x in $La_{1-x}Gd_xPO_4$ (also see Fig. S15), which is attributed to the increased activation energy for the hole release from the Pr^{3+} hole capturing centre as a result of valence band lowering by increasing x. Similar to Pr^{3+}, Tb^{3+} as a shallow hole capturing centre also gives a systemic shifting of TL glow peak IIIa in $La_{1-x}Gd_xPO_4$:0.002Bi^{3+}, 0.005Tb^{3+}, 0.005Nd^{3+} in Fig. 11a7)–a11). Note that the glow peaks IIIa and IIIb become broader in the solid solutions compared with that of $LaPO_4$ and $GdPO_4$, suggesting a broader trap distribution. This indicates that the VRBE at the valence band top exhibits site-to-site fluctuations based on the statistics in $La_{1-x}Gd_xPO_4$ when La is replaced by Gd. Particularly, for x from 0.25 to 0.75 in Fig. 11a8)–a10), the broad IIIa glow peak covers the room temperature (295 K) range, which results in the Nd^{3+} SWIR afterglow as shown in Fig. 12. Upon thermal stimulation at RT, the shallow Tb^{4+} hole trap spontaneously liberates holes to recombine with electrons at Bi^{2+}, producing Bi^{3+} in its excited state followed by Nd^{3+} SWIR persistent luminescence as a result of energy transfer from Bi^{3+}.

Fig. 9b), as another illustrating example, shows the stacked VRBE diagram for $Gd_{1-x}La_xAlO_3$ solid solutions where one can also engineer the hole trap depths of Tb^{3+} and Pr^{3+} by increasing x [49]. By combining Bi^{3+} with Tb^{3+} or Pr^{3+}, the holes trapped at Tb^{4+} or Pr^{4+} are predicted to release at a lower temperature than the electrons trapped at Bi^{2+}. On recombination with Bi^{2+}, Bi^{3+} in its excited state is formed giving Bi^{3+} emission and also Nd^{3+} SWIR luminescence by energy transfer from Bi^{3+} to Nd^{3+}. Tuneable thermally stimulated Nd^{3+} SWIR emission is proposed through valence band engineering and using the possible energy transfer from Bi^{3+} to Nd^{3+} because the broad Bi^{3+} emission band at 300–680 in $GdAlO_3$ [56] and $LaAlO_3$ [21,57] overlaps with the Nd^{3+} 4f-4f excitation bands like in Fig. 2a). Note that Bi^{3+} can act both as electron and as hole capturing centre like in La-, Y-, and $LuPO_4$ [35], one may also engineer the hole release from Bi^{4+} and the recombination with the electrons at Bi^{2+} followed by Nd^{3+} SWIR emission via ET of $Bi^{3+} \rightarrow Nd^{3+}$ in Bi^{3+}-Nd^{3+}-codoped compounds.

5. Conclusions

Data from thermoluminescence, fluorescence decay curves, photoluminescence spectroscopy, and ideas from constructed VRBE schemes have been combined to demonstrate the concept of rational design of

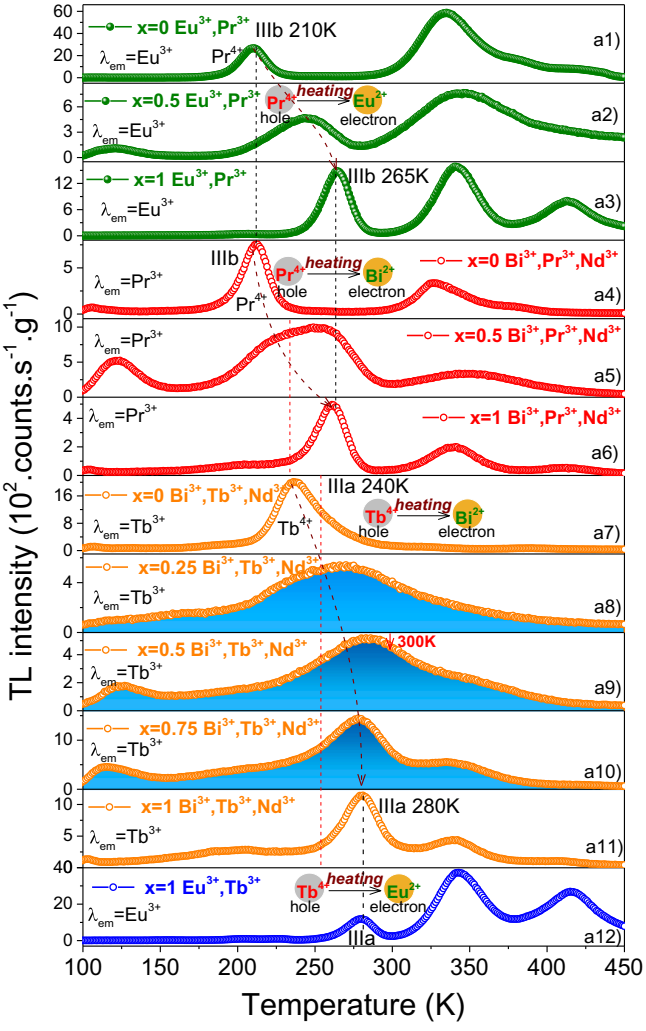

Fig. 11. Low-temperature TL glow curves for Bi^{3+} and/or Ln^{3+} doped $La_{1-x}Gd_xPO_4$ (x = 0–1) recorded at a heating of 1 K/s after 600 s β irradiation. A 600 nm bandpass filter 600FS40-50 was used to select Eu^{3+} emission in a1)–a3) and a12), and to monitor Pr^{3+} red emission in a4)–a6). A 550 nm bandpass 550FS40-50 was used to monitor Tb^{3+} green emission in a7)–a11). (For interpretation of the references to colour in this figure legend, the reader is referred to the web version of this article.)

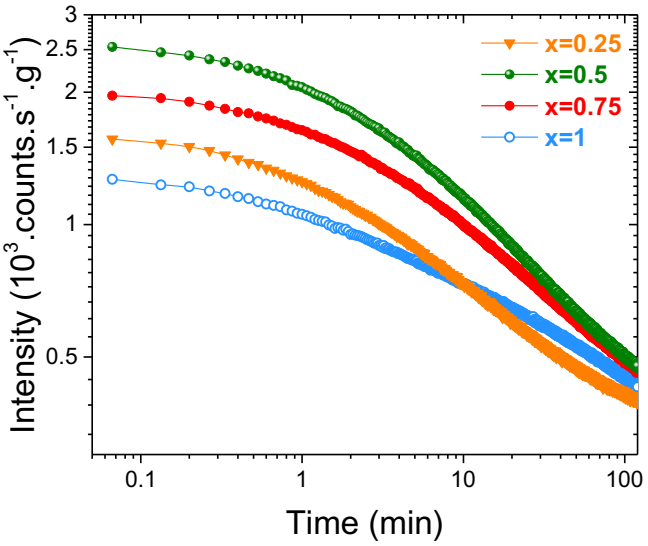

Fig. 12. Room temperature (295 K) isothermal decay curves after β irradiation while monitoring the emission from 400 to 900 nm for $La_{1-x}Gd_xPO_4$:0.002Bi^{3+}, 0.005Tb^{3+}, 0.005Nd^{3+}.

thermally stimulated Nd^{3+} luminescence between ~900–1700 nm. A new combination of using efficient energy transfer from Bi^{3+} to Nd^{3+} and using an adjustable hole trap depth via valence band engineering is presented in bismuth and lanthanides doped rare earth *ortho*-phosphate model compounds. We demonstrated that 1.06 μm Nd^{3+} photoluminescence can be realized by efficient energy transfer (ET) from Bi^{3+} to Nd^{3+} rather than by ET from Tb^{3+} to Nd^{3+} in YPO_4. The temperature of thermally stimulated Bi^{3+} emission needs then to be designed to further exploit the above energy transfer process from Bi^{3+} to Nd^{3+}. By combing ~2.7 eV deep Bi^{3+} electron trap with ~1.42 eV deep hole traps of Tb^{3+}, Pr^{3+}, or Bi^{3+} in ortho phosphate compounds the holes captured at Tb^{4+}, Pr^{4+}, or Bi^{4+} liberate at a lower temperature than that of electrons captured at Bi^{2+}. On recombination with Bi^{3+}, Bi^{3+} in its excited state is formed producing Bi^{3+} A-band emission and also owing to energy transfer from Bi^{3+} to Nd^{3+} the SWIR Nd^{3+} $^4F_{3/2} \rightarrow {}^4I_j$ (j = 9/2, 11/2, 13/2) emissions appear in YPO_4:0.005Bi^{3+}, 0.005Nd^{3+} and YPO_4:0.005Bi^{3+}, 0.005Ln^{3+}, 0.005Nd^{3+} (Ln = Tb and Pr). Here, the thermally stimulated Nd^{3+} SWIR emission is obtained by means of hole release rather than the more commonly reported electron release. We demonstrated that the temperature when thermally stimulated Nd^{3+} 1.06 μm emission appears can be tailored by valence band engineering in $Y_{1-x}Lu_xPO_4$ and $La_{1-x}Gd_xPO_4$, resulting in Tb^{3+} and Pr^{3+} hole trap depth changing. The tailoring was demonstrated for $Y_{1-x}Lu_xPO_4$ and $La_{1-x}Gd_xPO_4$ but can equally well be applied to other compounds like the solid solutions $Gd_{1-x}La_xAlO_3$. Our work shows a new general technique to deep understand afterglow mechanisms and to the rational design of SWIR afterglow phosphors by a new combination of efficient energy transfer from Bi^{3+} to Nd^{3+} and using adjustable hole release processes by valence band engineering. This work also opens the avenue to motivate scientists to explore novel SWIR afterglow phosphors in a design way instead of by trial and error approach.

Acknowledgements

T. Lyu thanks the financial support from the Chinese Scholarship Council for his PhD research (Tianshuai Lyu: 201608320151). We acknowledge Evert. P. J. Merkx from the Delft University of Technology for supporting the recording of the photoluminescence excitation spectra of Nd^{3+}-doped YPO_4 crystals using the OPO laser beam.

Appendix A. Supplementary data

Supplementary data to this article can be found online at https://doi.org/10.1016/j.cej.2019.04.125.

References

[1] S.W.S. McKeever, Thermoluminescence of Solids, Cambridge University Press, Cambridge, 1985.
[2] R. Chen, S.W. McKeever, Theory of Thermoluminescence and Related Phenomena, World Scientific, 1997.
[3] A.J.J. Bos, Thermoluminescence as a research tool to investigate luminescence mechanisms, Materials 10 (2017) 1357.
[4] Y. Zhang, R. Huang, H. Li, D. Hou, Z. Lin, J. Song, Y. Guo, H. Lin, C. Song, Z. Lin, J. Robertson, Germanium substitution endowing Cr^{3+}-doped zinc aluminate phosphors with bright and super-long near-infrared persistent luminescence, Acta Mater. 155 (2018) 214–221.
[5] T. Matsuzawa, Y. Aoki, N. Takeuchi, Y. Murayama, New long phosphorescent phosphor with high brightness, $SrAl_2O_4$:Eu^{2+}, Dy^{3+}, J. Electrochem. Soc. 143 (1996) 2670–2673.
[6] A.J.J. Bos, Theory of thermoluminescence, Radiat. Meas. 41 (2006) S45–S56.
[7] J. Xu, S. Tanabe, Persistent luminescence instead of phosphorescence: history, mechanism, and perspective, J. Lumin. 205 (2019) 581–620.
[8] Y. Zhuang, Y. Lv, L. Wang, W. Chen, T.-L. Zhou, T. Takeda, N. Hirosaki, R.-J. Xie, Trap depth engineering of $SrSi_2O_2N_2$:Ln^{2+}, Ln^{3+} (Ln^{2+} = Yb, Eu; Ln^{3+} = Dy, Ho, Er) persistent luminescence materials for information storage applications, ACS Appl. Mater. Interfaces 10 (2018) 1854–1864.
[9] Y. Li, M. Gecevicius, J. Qiu, Long persistent phosphors-from fundamentals to applications, Chem. Soc. Rev. 45 (2016) 2090–2136.
[10] H. Lin, B. Wang, Q. Huang, F. Huang, J. Xu, H. Chen, Z. Lin, J. Wang, T. Hu, Y. Wang, $Lu_2CaMg_2(Si_{1-x}Ge_x)_3O_{12}$:$Ce^{3+}$ solid-solution phosphors: bandgap engineering for blue-light activated afterglow applicable to AC-LED, J. Mater. Chem. C 4 (2016) 10329–10338.
[11] J. Wang, Q. Ma, Y. Wang, H. Shen, Q. Yuan, Recent progress in biomedical applications of persistent luminescence nanoparticles, Nanoscale 9 (2017) 6204–6218.
[12] T. Maldiney, A. Bessière, J. Seguin, E. Teston, S.K. Sharma, B. Viana, A.J.J. Bos, P. Dorenbos, M. Bessodes, D. Gourier, D. Scherman, C. Richard, The in vivo activation of persistent nanophosphors for optical imaging of vascularization, tumours and grafted cells, Nat. Mater. 13 (2014) 418–426.
[13] A.M. Smith, M.C. Mancini, S. Nie, Second window for in vivo imaging, Nat. Nanotechnol. 4 (2009) 710.
[14] D. Chen, J. Huang, T.J. Jackson, Vegetation water content estimation for corn and soybeans using spectral indices derived from MODIS near- and short-wave infrared bands, Remote Sens. Environ. 98 (2005) 225–236.
[15] A. Zhang, Z. Sun, M. Jia, G. Liu, F. Lin, Z. Fu, Simultaneous luminescence in I, II and III biological windows realized by using the energy transfer of $Yb^{3+} \rightarrow Er^{3+}/Ho^{3+} \rightarrow Cr^{3+}$, Chem. Eng. J. 365 (2019) 400–404.
[16] S. Zhou, N. Jiang, B. Zhu, H. Yang, S. Ye, G. Lakshminarayana, J. Hao, J. Qiu, Multifunctional bismuth-doped nanoporous silica glass: from blue-green, orange, red, and white light sources to ultra-broadband infrared amplifiers, Adv. Funct. Mater. 18 (2008) 1407–1413.
[17] G. Hong, J.T. Robinson, Y. Zhang, S. Diao, A.L. Antaris, Q. Wang, H. Dai, In vivo fluorescence imaging with Ag_2S quantum dots in the second near-infrared region, Angew. Chem. 124 (2012) 9956–9959.
[18] W. Fan, N. Lu, C. Xu, Y. Liu, J. Lin, S. Wang, Z. Shen, Z. Yang, J. Qu, T. Wang, S. Chen, P. Huang, X. Chen, Enhanced afterglow performance of persistent luminescence implants for efficient repeatable photodynamic therapy, ACS Nano 11 (2017) 5864–5872.
[19] J. Xu, D. Murata, Y. Katayama, J. Ueda, S. Tanabe, Cr^{3+}/Er^{3+} co-doped $LaAlO_3$ perovskite phosphor: a near-infrared persistent luminescence probe covering the first and third biological windows, J. Mater. Chem. B 5 (2017) 6385–6393.
[20] F. Liu, Y. Liang, Y. Chen, Z. Pan, Divalent nickel-activated gallate-based persistent phosphors in the short-wave infrared, Adv. Opt. Mater. 4 (2016) 562–566.
[21] R.H.P. Awater, P. Dorenbos, The Bi^{3+} 6s and 6p electron binding energies in relation to the chemical environment of inorganic compounds, J. Lumin. 184 (2017) 221–231.
[22] P. Dorenbos, A Review on how lanthanide impurity levels change with chemistry and structure of inorganic compounds, ECS J. Solid State Sci. Technol. 2 (2013) R3001–R3011.
[23] P. Dorenbos, Modeling the chemical shift of lanthanide 4f electron binding energies, Physical Review B 85 (2012) 165107.
[24] J. Ueda, S. Miyano, S. Tanabe, Formation of deep electron traps by Yb^{3+} codoping leads to super-long persistent luminescence in Ce^{3+}-doped yttrium aluminum gallium garnet phosphors, ACS Appl. Mater. Interfaces 10 (2018) 20652–20660.
[25] Z. Pan, Y.-Y. Lu, F. Liu, Sunlight-activated long-persistent luminescence in the near-infrared from Cr^{3+}-doped zinc gallogermanates, Nat. Mater. 11 (2012) 58–63.
[26] F. Liu, W. Yan, Y.-J. Chuang, Z. Zhen, J. Xie, Z. Pan, Photostimulated near-infrared persistent luminescence as a new optical read-out from Cr^{3+}-doped $LiGa_5O_8$, Sci. Rep. 3 (2013) 1554.
[27] Y. Li, S. Zhou, Y. Li, K. Sharafudeen, Z. Ma, G. Dong, M. Peng, J. Qiu, Long persistent and photo-stimulated luminescence in Cr^{3+}-doped Zn-Ga-Sn-O phosphors for deep and reproducible tissue imaging, J. Mater. Chem. C 2 (2014) 2657–2663.
[28] Y.-J. Liang, F. Liu, Y.-F. Chen, X.-J. Wang, K.-N. Sun, Z. Pan, New function of the Yb^{3+} ion as an efficient emitter of persistent luminescence in the short-wave

infrared, Light Sci. Appl. 5 (2016) e16124.
[29] N. Yu, F. Liu, X. Li, Z. Pan, Near infrared long-persistent phosphorescence in $SrAl_2O_4:Eu^{2+}$, Dy^{3+}, Er^{3+} phosphors based on persistent energy transfer, Appl. Phys. Lett. 95 (2009) 231110.
[30] J. Xu, D. Murata, J. Ueda, S. Tanabe, Near-infrared long persistent luminescence of Er^{3+} in garnet for the third bio-imaging window, J. Mater. Chem. C 4 (2016) 11096–11103.
[31] Y. Liang, F. Liu, Y. Chen, X. Wang, K. Sun, Z. Pan, Extending the applications for lanthanide ions: efficient emitters in short-wave infrared persistent luminescence, J. Mater. Chem. C 5 (2017) 6488–6492.
[32] Y. Liang, F. Liu, Y. Chen, X. Wang, K. Sun, Z. Pan, Red/near-infrared/short-wave infrared multi-band persistent luminescence in Pr^{3+}-doped persistent phosphors, Dalton Trans. 46 (2017) 11149–11153.
[33] J. Xu, S. Tanabe, A.D. Sontakke, J. Ueda, Near-infrared multi-wavelengths long persistent luminescence of Nd^{3+} ion through persistent energy transfer in Ce^{3+}, Cr^{3+} co-doped $Y_3Al_2Ga_3O_{12}$ for the first and second bio-imaging windows, Appl. Phys. Lett. 107 (2015) 081903.
[34] T. Lyu, P. Dorenbos, Charge carrier trapping processes in lanthanide doped $LaPO_4$, $GdPO_4$, YPO_4, and $LuPO_4$, J. Mater. Chem. C 6 (2018) 369–379.
[35] T. Lyu, P. Dorenbos, Bi^{3+} acting both as an electron and as a hole trap in La-, Y-, and $LuPO_4$, J. Mater. Chem. C 6 (2018) 6240–6249.
[36] F. You, A.J.J. Bos, Q. Shi, S. Huang, P. Dorenbos, Thermoluminescence investigation of donor (Ce^{3+}, Pr^{3+}, Tb^{3+}) acceptor (Eu^{3+}, Yb^{3+}) pairs in $Y_3Al_5O_{12}$, Phys. Rev. B 85 (2012) 115101.
[37] R.H.P. Awater, L.C. Niemeijer-Berghuijs, P. Dorenbos, Luminescence and charge carrier trapping in YPO_4:Bi, Opt. Mater. 66 (2017) 351–355.
[38] P. Dorenbos, Charge transfer bands in optical materials and related defect level location, Opt. Mater. 69 (2017) 8–22.
[39] D.L. Dexter, J.H. Schulman, Theory of concentration quenching in inorganic phosphors, J. Chem. Phys. 22 (1954) 1063–1070.
[40] M. Jiao, Y. Jia, W. Lu, W. Lv, Q. Zhao, B. Shao, H. You, $Sr_3GdNa(PO_4)_3F:Eu^{2+}$, Mn^{2+}: a potential color tunable phosphor for white LEDs, J. Mater. Chem. C 2 (2014) 90–97.
[41] A.J.J. Bos, P. Dorenbos, A. Bessière, A. Lecointre, M. Bedu, M. Bettinelli, F. Piccinelli, Study of TL glow curves of YPO_4 double doped with lanthanide ions, Radiat. Meas. 46 (2011) 1410–1416.
[42] M. Puchalska, P. Bilski, GlowFit—a new tool for thermoluminescence glow-curve deconvolution, Radiat. Meas. 41 (2006) 659–664.
[43] J. Azorín, Determination of thermoluminescence parameters from glow curves—I. A review, Int. J. Radiat. Appl. Instrumentation. Part D. Nucl. Tracks Radiat. Meas. 11 (1986) 159–166.
[44] W. Hoogenstraaten, Electron traps in zinc–sulphide phosphors, Philips Res. Rep 13 (1958) 515–693.
[45] R. Chen, S.A.A. Winer, Effects of various heating rates on glow curves, J. Appl. Phys. 41 (1970) 5227–5232.
[46] A.J.J. Bos, P. Dorenbos, A. Bessière, B. Viana, Lanthanide energy levels in YPO_4, Radiat. Meas. 43 (2008) 222–226.
[47] W. Jean-François, M. Ali, T.-B. Wan-Ü Lydia, C. Norbert, L. Omar, S. Nissan, S. Jack, Analysis of the free ion Nd^{3+} spectrum (Nd IV), J. Phys. B: At. Mol. Opt. Phys. 40 (2007) 3957–3972.
[48] T. Hoshina, S. Kuboniwa, 4f–5d Transition of Tb^{3+} and Ce^{3+} in MPO_4 (M = Sc, Y and Lu), J. Phys. Soc. Jpn. 31 (1971) 828–840.
[49] H. Luo, A.J.J. Bos, P. Dorenbos, Controlled electron-hole trapping and detrapping process in $GdAlO_3$ by valence band engineering, J. Phys. Chem. C 120 (2016) 5916–5925.
[50] R.H.P. Awater, P. Dorenbos, Towards a general concentration quenching model of Bi^{3+} luminescence, J. Lumin. 188 (2017) 487–489.
[51] A. Mraouefel, L. Guerbous, A. Boukerika, M. Diaf, A. Mendoud, M. Seraiche, M. Taibeche, M.S.E. Hamroun, N. Baadji, Effect of the vanadium concentration on structural and photoluminescence of $YP_{1-x}V_xO_4$: 1 at. % Tb^{3+} nanophosphors, Opt. Mater. 65 (2017) 129–136.
[52] A. Lecointre, A. Bessière, A.J.J. Bos, P. Dorenbos, B. Viana, S. Jacquart, Designing a red persistent luminescence phosphor: the example of $YPO_4:Pr^{3+}$, Ln^{3+} (Ln = Nd, Er, Ho, Dy), J. Phys. Chem. C 115 (2011) 4217–4227.
[53] P.W. Tasker, A.M. Stoneham, An appraisal of the molecular model for the Vk centre, J. Phys. Chem. Solids 38 (1977) 1185–1189.
[54] R. Gazzinelli, G.M. Ribeiro, M.L. de Siqueira, ESR and endor studies of the VK center in SrF_2, Solid State Commun. 13 (1973) 1131–1134.
[55] N.F. Mott, A.M. Stoneham, The lifetime of electrons, holes and excitons before self-trapping, J. Phys. C: Solid State Phys. 10 (1977) 3391.
[56] A.M. Srivastava, H.A. Comanzo, The ultraviolet and visible luminescence of Bi^{3+} in the orthorhombic perovskite, $GdAlO_3$, Opt. Mater. 63 (2017) 118–121.
[57] L.I. van Steensel, S.G. Bokhove, A.M. van de Craats, J. de Blank, G. Blasse, The luminescence of Bi^{3+} in $LaInO_3$ and some other perovskites, Mater. Res. Bull. 30 (1995) 1359–1362.